Chinese Chemical Letters 34 (2023) 107468

Contents lists available at ScienceDirect

Chinese Chemical Letters

journal homepage: www.elsevier.com/locate/cclet

Lattice expansion boosting photocatalytic degradation performance of $CuCo_2S_4$ with an inherent dipole moment

Yicheng Guo[1], Biguo Yan[1], Fang Deng*, Penghui Shao, Jianping Zou, Xubiao Luo, Shuqu Zhang, Xibao Li*

National-Local Joint Engineering Research Center of Heavy Metal Pollutants Control and Resource Utilization, Nanchang Hangkong University, Nanchang 330063, China

ARTICLE INFO

Article history:
Received 28 December 2021
Revised 24 April 2022
Accepted 24 April 2022
Available online 28 April 2022

Keywords:
$CuCo_2S_4$
Lattice distortion
Visible-light photocatalysis
Structure-activity relationship
Biodegradability improvement

ABSTRACT

Realizing efficient charge separation and directional transfer is a challenge for single-component semiconductors. The spatial electric field generated by dipole moment could promote charge separation. Here, three-dimensional hierarchical $CuCo_2S_4$ microspheres with lattice distortion were prepared, and lattice distortion was modulated by changing feed Co/Cu molar ratios in synthesis. $CuCo_2S_4$ showed asymmetric crystal structure, leading to generation of dipole moment. The charge separation efficiency of $CuCo_2S_4$ was related to lattice distortion, and lattice expansion was in favor for charge separation. The $CuCo_2S_4$ with feed Cu/Co molar ratio of 1:4 (CCS-4) showed the maximum lattice expansion and exhibited the highest photocatalytic activity, which was attributable to the highest charge separation efficiency and the largest specific surface area. CCS-4 can remove 95.4% of tetracycline hydrochloride within 40 min photocatalysis, and effectively improve the biodegradability of pharmaceutical wastewater. Importantly, this study provides a new vision for constructing single-component photocatalysts with high photocatalytic performance.

Antibiotics have been massively produced, and are widely used in treatment of bacterial infections in animals and humans, leading to their emission to environment matrixes [1–4]. Shockingly, antibiotics have been ubiquitously detected in rivers, lakes, oceans and even in drinking water, which pose unpredictable risks to ecological environment and human health due to the reproduction of antibiotic-resistant bacteria and genes [5–9]. To aim at eliminating antibiotics in aquatic environment, various approaches such as activated sludges [10,11], microfiltration [12,13], adsorption [14,15] and photocatalysis have been proposed [16–20]. Among them, photocatalysis has received considerable interest owing to its incomparable advantages of easy operation, high performance and low cost [21–25]. The photocatalytic process includes three main steps: light energy absorption, photogenerated charge separation and surface reaction. The photocatalytic activity is directly affected by light absorption and effective separation of photogenerated charges [26–30]. Nevertheless, traditional single-component photocatalysts usually suffer from low utilization of solar light, disordered migration and easy recombination of photogenerated charge carriers on spatial scale [31–35]. Accordingly, the key issue is how to design single-component photocatalyst with high visible-light response and efficient separation of photogenerated charge carriers.

It is well known that dipole moment in tetrahedral or octahedral structure of oxide unit plays an important part in photocatalytic process, because internal electric field formed by dipole moment is conducive to separation of photogenerated electrons (e^-) and holes (h^+) [36]. For example, deformed TiO_6 octahedron in the pentagonal prism tunnel and zigzag layer structure of $BaTi_4O_9$ will generate dipole moment, which effectively promotes separation and migration of photogenerated e^- and h^+ [37]. Such structure-activity relationship also holds for other oxide or nitride semiconductors with crystal unit of tetrahedron or octahedron [38]. Lattice distortion and resulted dipole moment can be achieved through strain in piezoelectric materials, such as MoS_2 [39,40] and $BaTiO_3$ [41], and some studies indicate that lattice distortion also has certain effect on charge separation, and influences the creation of active catalytic centers [42]. However, rational design of dipole moment and lattice distortion of semiconductor, and the role of lattice distortion in regulation of photocatalytic activity are still highly controversial [43]. Therefore, it is very meaningful to explore how dipole moment and lattice distortion influence the reactivity for the development of high-performance photocatalysts.

* Corresponding authors.
E-mail addresses: dengfang40030@126.com (F. Deng), lxbicf@126.com (X. Li).
[1] These authors contributed equally to this work.

https://doi.org/10.1016/j.cclet.2022.04.066
1001-8417/

$CuCo_2S_4$ is a ternary transition metal sulfide with cubic spinel structure (space group *Fd*-3 m), in which Cu and Co occupy the tetrahedral and octahedral sites, respectively [44,45]. It has been drawn extensive attention as an efficient photocatalyst due to its better electrochemical performance, higher electrical conductivity and stability than the corresponding ternary metal oxides and binary metal sulfides [46]. More interestingly, its cubic spinel structure provides a potential to have dipole moment by avoiding overlapping of positive and negative charge centers, which could create internal electric field for driving bulk and surface charge separation [47]. In addition, the effect of lattice shrinkage and expansion on the photocatalytic properties of $CuCo_2S_4$ remains unclear.

Herein, three-dimensional hierarchical $CuCo_2S_4$ microspheres with asymmetric crystal structure were prepared, and lattice distortion was modulated by changing the feed Co/Cu molar ratio in synthesis. Lattice distortion in $CuCo_2S_4$ can be discovered by theoretical calculation and moiré fringes in high-resolution transmission electron microscopy (HRTEM), and a qualitative analysis through modeling illustrates that $CuCo_2S_4$ has polar surface. The charge separation efficiency and photocatalytic activity were significantly enhanced *via* lattice expansion. The systematical study on dipole moment and lattice distortion has important realistic significance for understanding the intrinsic driving force of charge separation and regulating photocatalytic activity of single-component photocatalysts.

One-step solvothermal synthesis of $CuCo_2S_4$. 1 mmol $CuCl_2{\cdot}2H_2O$, 6 mmol thiourea and 2 mmol $CoCl_2{\cdot}6H_2O$ were added to 60 mL mixture solvent of ethylene glycol and ultrapure water (volume ratio = 1:1), and was stirred at ambient conditions for 40 min. The mixed solution reacted in 100 mL stainless steel Teflon-lined autoclave at 180 °C for 24 h. The obtained black powder was collected, purified with absolute ethanol and deionized water, and dried at 60 °C. This product with feed Co/Cu molar ratio of 2:1 was marked as CCS-2. Similarly, $CuCo_2S_4$ samples with feed Co/Cu molar ratios of 3, 4 and 5 were marked as CCS-3, CCS-4 and CCS-5, respectively.

The visible-light photocatalytic performance of $CuCo_2S_4$ was studied by degrading tetracycline hydrochloride (TC) in a reactor with reflux condensing unit under the irradiation of 300 W xenon lamp (PLS-SXE300, Beijing Perfectlight) with 400 nm cut-filter. The experimental procedure is listed as follows: a certain amount of $CuCo_2S_4$ was added to 100 mL TC solution, and the suspension was placed in a dark box under continuous magnetic stirring for 40 min to ensure adsorption equilibrium. Then the suspension was irradiated with visible light. At interval of 20 min, 3 mL of suspension was taken out from reactor, and was instantly filtered with 0.22 μm filter to obtain a clear filtrate. The TC concentration change in filtrate was monitored using UV–vis spectrophotometer (Hitachi, Japan) at $\lambda = 357$ nm. The intermediates of TC were analyzed by high-performance liquid chromatography-mass spectrometry (HPLC-MS).

The mineralization of TC was carried out by adding 250 mg $CuCo_2S_4$ in 100 mL of 50 mg/L TC. The operating procedures were the same as the above. The filtrate was diluted 5 times with deionized water, and then analyzed on Shimadzu TOC-L total organic carbon (TOC) analyzer.

The active species were detected by adding isopropyl alcohol (IPA), triethanolamine (TEOA) and *p*-benzoquinone (BQ) to the above photocatalytic system as the trapping agents of hydroxyl radicals ($^{\bullet}OH$), hole (h^+) and superoxide radicals ($O_2^{\bullet-}$), respectively. The operating procedures were the same as the above. The electron spin resonance (ESR) procedures was as follows: 10 mg $CuCo_2S_4$ samples were dispersed in 5 mL deionized water or methanol solution in sonic oscillator, then 200 μL of dispersion was taken out and mixed with 100 μL of 100 mmol/L 5,5-dimethyl-1-pyrroline-*N*-oxide (DMPO) solution, and then analyzed using ESR spectrometer under visible light and in absence of light.

The application of CCS-4 in pharmaceutical wastewater was carried out, and the operating procedures were essentially the same as mineralization experiment of TC. The clear filtrate was diluted 100 times, and then analyzed on Shimadzu TOC-L total organic carbon analyzer. The COD of filtrate was determined according to reference [48].

The crystal structure of $CuCo_2S_4$ with different feed Co/Cu molar ratios in synthesis was analyzed using powder X-ray diffraction (XRD) (Fig. S1a in Supporting information). The diffraction peaks at 26.6°, 31.3°, 38.0°, 47.0°, 49.9° and 54.8° can be ascribed to the (022), (113), (004), (224), (115) and (044) planes of $CuCo_2S_4$ cubic spinel phase (JCPDS No. 42–1450). The diffraction peak intensity of $CuCo_2S_4$ with a normal stoichiometric ratio is higher than that of cobalt-rich $CuCo_2S_4$, which is probably due to the superimposition of fluorescent X-rays generated by Co element on the background of diffraction pattern [49].

The chemical composition and atomic bonding state of $CuCo_2S_4$ were further analyzed by X-ray photoelectron spectroscopy (XPS). The characteristic peaks of Cu, Co and S elements appear in the XPS survey spectra (Fig. S1b in Supporting information). Moreover, the peaks of C and O elements were also observed due to adsorbed oxygen and organic sulfur precursor. In high-resolution XPS spectra of Co 2p, two characteristic peaks of Co 2p, Co $2p_{2/3}$ and Co $2p_{1/2}$ were observed, of which the Co^{3+} doublet is located at 778.8 and 794.0 eV with a fission value of 15.2 eV, and the Co^{2+} doublet is located at 781.4 and 797.8 eV with a fission value of 16.4 eV [50]. In addition, two satellite peaks of Co 2p were observed at 785.5 and 802.8 eV (Fig. S1c in Supporting information). The peaks of Cu $2p_{1/2}$ and Cu $2p_{3/2}$ are located at 952.4 and 932.6 eV, respectively. Moreover, the satellite peak of Cu 2p was observed at 956.2 eV (Fig. S1d in Supporting information). The binding energies of S 2p peak at 161.3 eV ($2p_{3/2}$) and 162.4 eV ($2p_{1/2}$) indicate that the valence of S is −2 (Fig. S1e in Supporting information). The satellite peak of S 2p at 168.9 eV indicates that S has a strong interaction with the oxygen adsorbed on the surface.

Micro-morphologies of $CuCo_2S_4$ (CCS-2 and CCS-4) were observed using SEM and TEM (Fig. 1). CCS-2 and CCS-4 consist of three-dimensional hierarchical microspheres with uniform size of

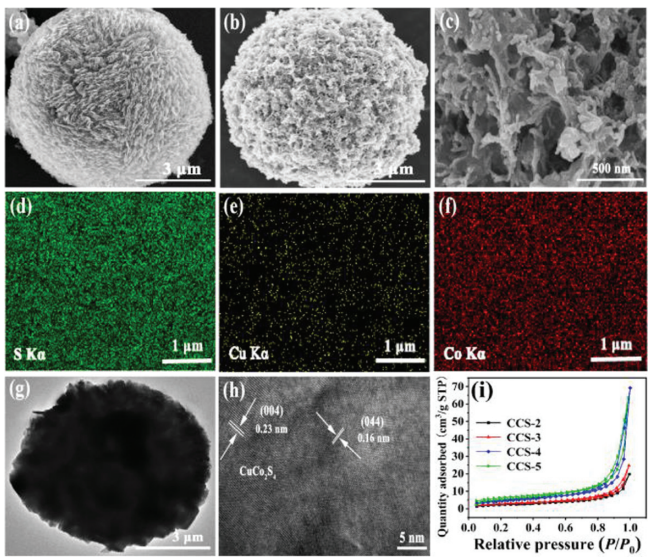

Fig. 1. (a) SEM image of CCS-2. (b, c) SEM images of CCS-4 at different magnifications. (d-f) Elemental mapping micrograph of CCS-4. (g) TEM of CCS-4. (h) HRTEM of CCS-4. (i) N_2 adsorption-desorption isotherms of $CuCo_2S_4$ with different feed Cu/Co molar ratios.

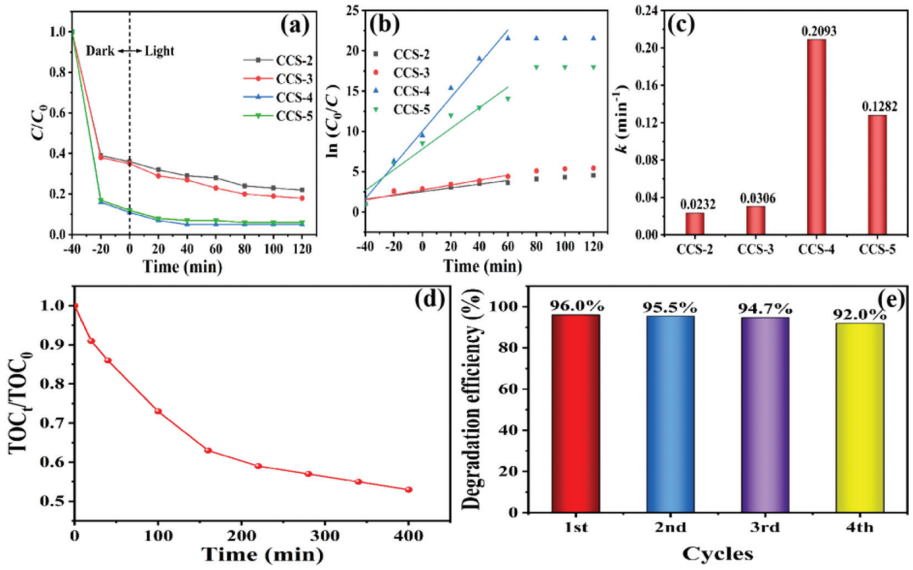

Fig. 2. (a) Photocatalytic degradation of TC by $CuCo_2S_4$ with different Cu/Co molar ratios under visible light irradiation, (b) fitting curves of first-order reaction kinetics and (c) first-order reaction rate constant. (d) TOC removal of TC with photocatalytic time (the initial concentration of TC: 50 mg/L). (e) Stability of CCS-4.

about 10 μm, and there are many pores on their surface. The element mapping of CCS-4 confirms even distribution of S, Co and Cu elements in the sample. TEM images further illustrate porous microsphere of CCS-4. In the HRTEM image of CCS-4, the lattice fringes with distances of 0.23 and 0.16 nm are consistent with (004) and (044) planes of $CuCo_2S_4$, respectively (Fig. 1h). The above results indicate successful synthesis of three-dimensional $CuCo_2S_4$ hierarchical microspheres.

The pore structure and surface area are important parameters for adsorption and catalysis. The isothermal curves of all the $CuCo_2S_4$ samples (Fig. 1i) belong to type IV, and exhibit H3 type hysteresis loop, indicating their mesoporous structure. The pore size distribution mainly ranges from 2 nm to 50 nm (Fig. S2 in Supporting information). The surface areas of CCS-2, CCS-3, CCS-4 and CCS-5 are 8.59, 10.49, 22.20 and 17.40 m^2/g, respectively (Table S1 in Supporting information). The pore parameters were also listed in Table S1.

The photocatalytic condition was optimized (Fig. S3 in Supporting information), and the visible-light photocatalytic performance of $CuCo_2S_4$ with different feed Cu/Co molar ratios was evaluated by degrading TC under the optimal experimental conditions (50 mg photocatalysts, 10 mg/L TC solution at initial pH 4.65). All the $CuCo_2S_4$ samples showed high adsorption capacity for TC, which could be attributed to many obvious micropores on the surface of the microspheres. The photocatalytic activity of CCS samples increased as followed: CCS-2 (78.1%) < CCS-3 (81.7%) < CCS-5 (94.4%) < CCS-4 (95.4%), indicating that the feed Cu/Co molar ratios in the synthesis have great influence on photocatalytic performance of $CuCo_2S_4$. The photocatalytic activity of CCS-5 (94.4%) is almost the same as that of CCS-4 (95.4%), which is probably due to the similar separation of photogenerated charge carriers, and similar adsorption capacity for TC (Fig. 2a). TC concentration did not change after 60 min in case of CCS-4 and CCS-5, thus the kinetic data for TC degradation within 60 min were fitted using first-order reaction kinetics equation (Eq. 1, Fig. 2b) [51]

$$\ln\left(\frac{C_0}{C}\right) = kt \quad (1)$$

where C_0 is initial concentration of TC, C is the TC concentration sampled at time t, and k is the first-order reaction rate constant. The regression curves of $\ln(C_0/C_t)$ *versus* t indicated that TC degradation by photocatalysis of $CuCo_2S_4$ can conform with first-order reaction kinetics equation [52,53]. The k values of TC degradation over $CuCo_2S_4$ samples can be determined from the slope of fitting lines from −40 min to 60 min, and the k values were listed in Fig. 2c. Compared with the reported $CuCo_2S_4$-based photocatalysts [54–56], the $CuCo_2S_4$ with lattice expansion in this study shows excellent photocatalytic activities (Table S2 in Supporting information). Moreover, the $CuCo_2S_4$ samples in this study can be comparable to other photocatalysts such as TiO_2 and g-C_3N_4 (Table S2) [50,57–59].

As the reaction goes on, the intensity of the absorption peak at 358.4 nm decreases. Moreover, there is red-shift of the maximum absorption peak position (Fig. S4 in Supporting information), indicating the formation of intermediate products. The degradation intermediates of TC were analyzed by HPLC-MS (Fig. S5 in Supporting information). According to HPLC-MS analysis, TC degradation followed two possible pathways. TC underwent the detachment of *N*-methyl group, dehydroxylation, deamination, addition reaction and ring-opening reaction to generate intermediates during photocatalytic process (Fig. S6 in Supporting information), and partial intermediates were further degraded and mineralized to CO_2 and H_2O, which was supported by TOC results. With the photocatalysis going on, TOC value of TC solution generally decreased, and TOC removal efficiency reached 47.6% after 400 min photocatalysis by CCS-4 (Fig. 2d). The toxicity of tetracycline and its intermediates was analyzed by ECOSAR software (Table S3 in Supporting information). Overall, the toxicity was sharply reduced with the photocatalysis going on.

To test the stability of $CuCo_2S_4$, four cyclic runs of TC degradation over CCS-4 were carried out. CCS-4 did not show obvious decrease of photocatalytic activity in TC degradation after four repeated runs, indicating high stability of CCS-4 (Fig. 2e).

The establishment of structure-activity relationship will facilitate discovering insights into photocatalytic mechanism of $CuCo_2S_4$, thus the relationship among specific surface area, light absorption characteristics, charge separation and photocatalytic activity were systematically investigated. The photocatalytic activity of $CuCo_2S_4$ samples with different feed ratios of Co/Cu has similar change trend with their specific surface area (Fig. S7a in Supporting information), indicating that large specific surface area is a positive factor for photocatalytic degradation of TC. $CuCo_2S_4$ samples

have visible light absorption, and CCS-4 has the strongest light response among these samples (Fig. S7b in Supporting information). The band gap energy (E_g) of $CuCo_2S_4$ can be calculated using Tauc formula (Eq. 2):

$$(\alpha h\nu)^2 = A(h\nu - E_g) \quad (2)$$

where α and ν are the absorption coefficient and light frequency, respectively. *h is* Planck constant. The E_g values were determined by prolonging the linear part of $(\alpha h\nu)^2$ *versus* $h\nu$ curves to $(\alpha h\nu)^2 = 0$ (Fig. S7c in Supporting information). The redox ability of photocatalysts is affected by valence band (VB) and conduction band (CB) position, thus the CB and VB of $CuCo_2S_4$ were determined according to Mott-Schottky curves and calculation. According to the positive slope of the linear part of Mott-Schottky curves (Fig. S7d in Supporting information), $CuCo_2S_4$ samples are n-type semiconductor. The flat band potential (V_{fb}) values *vs.* $E_{Ag/AgCl}$ can be determined by extrapolating the linear part to $C^{-2} = 0$. The E_{CB} and E_{VB} can be calculated using following equations: V_{fb} (*vs.* NHE) = V_{fb} (*vs.* $E_{saturated\ Ag/AgCl}$) + 0.2; $E_{CB} = V_{fb}$ (*vs.* NHE) – 0.1 [60]; $E_{CB} = E_{VB} - E_g$, and the related parameters were summarized in Table 1.

The charge separation of $CuCo_2S_4$ was characterized by photoluminescence (PL) and photocurrent. The PL decreased with the following order: CCS-2 > CCS-3 > CCS-5 > CCS-4 (Fig. S8 in Supporting information). The lowest PL intensity of CCS-4 indicated its lowest photogenerated e^--h^+ recombination rate in all samples, which was conducive to the improvement of photocatalytic performance. Photocurrent also can reflect separation degree of photogenerated e^- and h^+, thus the photocurrent intensity of $CuCo_2S_4$ with different feed Co/Cu molar ratios was determined (Fig. S7e in Supporting information). All the $CuCo_2S_4$ samples had significant photocurrent response, and the photocurrent intensity of $CuCo_2S_4$ samples increased with following order: CCS-4 > CCS-5 > CCS-3 > CCS-2. The highest photocurrent intensity of CCS-4 indicated the highest separation efficiency of photogenerated e^- and h^+. The decay in photocurrent of $CuCo_2S_4$ with time is probably due to its unstable sensitivity to light. The electrochemical impedance spectra (EIS) are important tools for studying charge transfer dynamics [61,62]. The smaller arc radius of impedance spectrum indicated more efficient transfer of photogenerated e^--h^+ pairs. The impedance arc radius of $CuCo_2S_4$ decreased as followed: CCS-4 > CCS-5 > CCS-3 > CCS-2 (Fig. S7f in Supporting information). The smallest arc radius of CCS-4 further indicated the fastest charge transfer speed. The highest photocatalytic performance CCS-4 can be attributed to the largest specific area, the strongest visible-light absorption, and the most efficient separation and transfer of photogenerated e^- and h^+.

Studies have shown that single-component semiconductor usually exhibits unsatisfactory photocatalytic performance owing to ineffective separation of photogenerated e^- and h^+. In fact, pure $CuCo_2S_4$ (CCS-4 and CCS-5) samples show excellent visible-light photocatalytic performance in our study. Despite the structure, light absorption, and charge separation and transfer have been identified as important factors for the excellent photocatalytic performance of $CuCo_2S_4$, one fundamental question still remains mysterious: What kind of crystal configurations of $CuCo_2S_4$ that predominates structure, light absorption, and charge separation and transfer?

To reveal the mystery, crystal structure of $CuCo_2S_4$ was analyzed. The $CuCo_2S_4$ has a spinel cubic crystal structure according to XRD analysis. The crystal structure model of $CuCo_2S_4$ and four possible end structure models on the (113) crystal plane were constructed using Diamond drawing software. The lattice structure of $CuCo_2S_4$ is shown in Figs. S9a and b (Supporting information). $CuCo_2S_4$ belongs to space group of cubic *Fd*-3 m. Copper atoms occupy the tetrahedral sites, and cobalt atoms occupy octahedral sites. The unit cell parameters of $CuCo_2S_4$ samples with different feed Cu/Co molar ratios were calculated based on the characteristic parameters of cubic crystal structure [63], the interplanar spacing formula [64] and the Bragg equation (Eqs. 3–6) [65]:

$$a = b = c,\ \alpha = \beta = \gamma = 90^\circ \quad (3)$$

$$d = \frac{a}{\sqrt{h^2 + k^2 + l^2}} \quad (4)$$

$$2d \sin\theta = n\lambda \quad (5)$$

$$a = \frac{\lambda}{2\sin\theta}\sqrt{h^2+k^2+l^2} \quad (6)$$

where a, b and c are the edge lengths of unit cell; α, β and γ are the angles of intersection between the edges, d is the distance between the crystal planes, (hkl) is the crystal face index, n is the number of reflection orders, θ is the angle between the incident ray and crystal plane and λ is the X-ray wavelength. The average grain size (D) of $CuCo_2S_4$ samples with different feed Co/Cu molar ratios were calculated using Scherrer formula (Eq. 7) [66]:

$$D = \frac{k\lambda}{B\cos\theta} \quad (7)$$

where k, B and θ is the Schiller constant (the general value is 0.89), half-height width of the diffraction peak and the diffraction angle, respectively. The calculated unit cell parameters and average grain size of $CuCo_2S_4$ samples with different feed Co/Cu molar ratios were listed in Table 2. As is seen from Table 2, the lattice constants of $CuCo_2S_4$ samples can be regulated *via* nonstoichiometric control, and the lattice constants of $CuCo_2S_4$ increased with increasing Co/Cu molar ratio from 2 to 4, and then decreased with further increasing Co/Cu molar ratio. The CCS-4 sample has the largest lattice constant. The cell parameters (a = 9.485 Å) of CCS-4 are larger than that in previous report (a = 9.482 Å) [67] and that of standard cubic $CuCo_2S_4$ (a = 9.474 Å) [68]. According to the above analysis, we envisaged lattice distortion of $CuCo_2S_4$. Thereby, the relationship between change rate of lattice constant and the reciprocal of average grain size ($1/D$) was studied. The rate of change of lattice constant was calculated using the following Eq. 8:

$$Rate\ of\ change = \frac{a - a_0}{a_0} \times 100\% \quad (8)$$

where a is the lattice constant of $CuCo_2S_4$ samples, and a_0 = 9.474. Fig. S9c (Supporting information) shows the relationship between the rate of change of lattice constant and $1/D$. The values of rate

Table 1
E_g, E_{CB} and E_{VB} values of $CuCo_2S_4$ samples.

Samples	E_g (eV)	V_{fb} *vs.* $E_{saturated\ Ag/AgCl}$ (V)	V_{fb} *vs.* NHE (V)	E_{CB} (eV)	E_{VB} (eV)
CCS-2	1.58	−0.55	−0.35	−0.45	1.13
CCS-3	1.52	−0.51	−0.31	−0.41	1.11
CCS-4	1.40	−0.58	−0.38	−0.48	0.92
CCS-5	1.88	−0.54	−0.34	−0.44	1.44

Table 2
Cell parameters, lattice distortion (δ_d/d), lattice constant change rate and average grain size (D) of $CuCo_2S_4$ samples.

$CuCo_2S_4$	a	b	c	δ_d/d	$(a\text{-}a_0)/a_0$	D (nm)
CCS-2	9.461	9.461	9.461	−0.013	−0.13	29.8
CCS-3	9.473	9.473	9.473	−0.107	−0.01	26.4
CCS-4	9.485	9.485	9.485	0.017	0.11	20.9
CCS-5	9.480	9.480	9.480	0.052	0.06	25.7

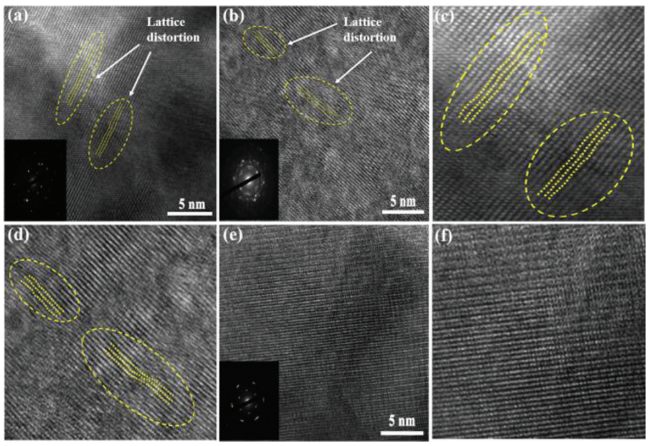

Fig. 3. HRTEM images of CCS-2 (a), CCS-3 (b) and CCS-4 (c) with corresponding selected area electron diffraction (SAED) in the lower left corner. (d-f) The enlarged images of the selected area in (a-c).

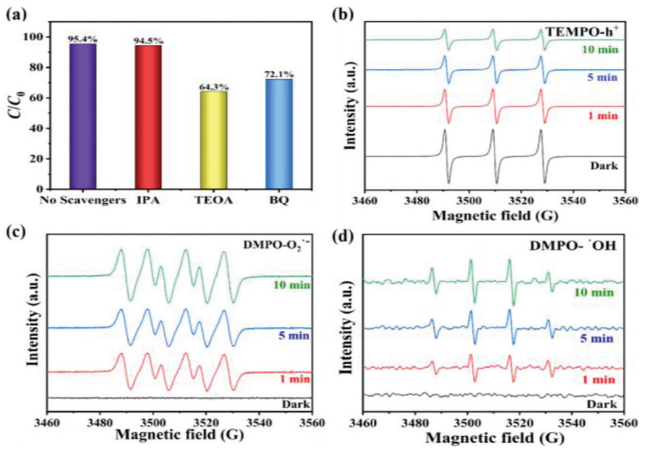

Fig. 4. (a) The effect of different scavengers on the photocatalytic degradation of TC by CCS-4. (b) ESR spectrum of h^+ captured by TEMPO. (c) ESR spectrum of $O_2^{\bullet-}$ captured by DMPO. (d) ESR spectrum of $^{\bullet}OH$ captured by DMPO.

of change *versus* $1/D$ of CCS-4 and CCS-5 are larger than 0, indicating lattice expansion of CCS-4 and CCS-5, while those of CCS-2 and CCS-3 are less than 0, indicating lattice shrinkage of CCS-2 and CCS-3. As shown in Fig. S9d (Supporting information), the photocatalytic activity of $CuCo_2S_4$ is in tune with the lattice distortion. $CuCo_2S_4$ with larger lattice expansion shows higher the photocatalytic activity. Contrarily, the larger lattice shrinkage leads to lower photocatalytic activity.

The lattice distortion (δ_d/d) was also calculated using the following Eq. 9 [69]:

$$\frac{\delta d}{d} = \frac{\beta(2\theta)}{4\tan\theta} \tag{9}$$

where $\beta(2\theta)$ is the width of the 2θ diffraction peak. The calculated δ_d/d values were summarized in Table 2. The δ_d/d values of CCS-2 and CCS-3 are less than 0, which are manifested as lattice shrinkage. The δ_d/d values of CCS-4 and CCS-5 are greater than 0, manifesting lattice expansion.

To further confirm the existence of lattice distortion, the lattice distortion of $CuCo_2S_4$ was characterized by HRTEM along with selected area electron diffraction (SAED). In Figs. 3a and b, some local lattice distortions in the moiré fringes were observed. In the enlarged images of the area (Figs. 3c and d) marked by arrows in Figs. 3a and b, we can observe lattice distortion in a continuous direction [70]. In Figs. 3e and f, there is no obvious lattice fringe deformation. The above analysis indicated that CCS-2 and CCS-4 have lattice distortion, while CCS-3 has no obvious lattice distortion.

As far as the structure of the photocatalyst is concerned, the particle size and dipole moment will affect the separation efficiency of photogenerated e^--h^+ pairs. The small particle size is beneficial to reduce the migration distance of charge carriers, and the dipole moment is conducive to reduce the e^--h^+ recombination rate [71]. CCS-4 has the smallest granularity (Table 2). The most direct way to know whether a material has a dipole moment is to see whether its structure has a polar surface. In short, the polar surface depends on whether the internal atomic structure is symmetrical [72]. Here, a qualitative analysis on whether $CuCo_2S_4$ has polar surface was conducted through modeling. As shown in Fig. S10 (Supporting information), four possible terminal structures on the $CuCo_2S_4$ (113) surface were constructed. The atomic structure of Cu terminal, Co terminal and two S terminal models is asymmetrical (Figs. S10a–d), and the atomic structure of the multilayer terminal structure is also not symmetrical (Fig. S10e). The asymmetrical structure is enough to prove that the surface of $CuCo_2S_4$ (113) is polar, and $CuCo_2S_4$ have an inherent dipole

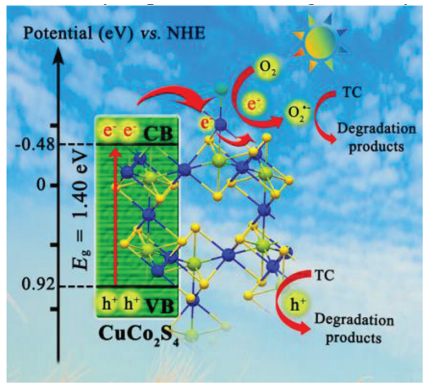

Scheme 1. Possible photocatalytic mechanism of $CuCo_2S_4$ in degradation of TC pollutants under visible light.

moment. Because $CuCo_2S_4$ itself has an inherent dipole moment, the occurrence of lattice distortion in $CuCo_2S_4$ will only affect its dipole [73]. The synergistic effect of internal dipole moments and lattice expansion explains why CCS-4 shows the highest charge separation efficiency and photocatalytic activity.

In order to explore the active species in TC degradation by photocatalysis of CCS-4, trapping experiment and electron spin resonance (ESR) were carried out. As shown in Fig. 4a, under visible-light irradiation, the degradation efficiency of TC was 95.4% in absence of sacrificial agents. After adding IPA, there is no change of TC degradation efficiency. The addition of triethanolamine (TEOA) and *p*-benzoquinone (BQ) in photocatalysis system leads to significant decline in TC degradation efficiency. Based on the results of trapping experiment, it can be inferred that h^+ and $O_2^{\bullet-}$ are major active species in degradation of TC. In the ESR spectra, three characteristic signal peaks of TEMPO-h^+ were observed (Fig. 4b). The peak signal intensity is the highest under dark conditions, but the intensity decreases with the increase of irradiation time, which is similar to the reported studies [74]. No DMPO-$O_2^{\bullet-}$ peaks are observed in the dark, while the characteristic signal peaks of DMPO-$O_2^{\bullet-}$ are observed and the peak intensity enhances with time of visible light irradiation (Fig. 4c). The characteristic signal peaks of DMPO-$^{\bullet}OH$ were also observed under visible light (Fig. 4d), while $^{\bullet}OH$ cannot be detected in the trapping experiment. According to the reactive species in the photocatalysis, energy band structure, lattice distortion and dipole moment, possible photocatalytic mechanism of CCS is inferred as followed (Scheme 1): Un-

der visible light, lattice distortion and dipole moment drive separation and transfer of e^- and h^+. The CB position (−0.44 eV) of CCS is more negative than the standard redox potential of $O_2/O_2^{\bullet-}$ (−0.33 eV *vs*. NHE), thus the photogenerated e^- in CB has ability to react with oxygen to generate $O_2^{\bullet-}$. The E_{VB} (0.92 eV) of CCS-4 is lower than the standard redox potential of $^{\bullet}OH/OH^-$ (1.99 eV *vs*. NHE), thus the photogenerated h^+ in VB cannot oxidize OH^- to generate $^{\bullet}OH$. The DMPO-$^{\bullet}OH$ peaks in ESR may put down to the formation of $^{\bullet}OH$ radicals *via* the route of $O_2^{\bullet-} \rightarrow H_2O_2 \rightarrow {}^{\bullet}OH$, and the reaction equations are as follows (Eqs. 10–12) [75]:

$$O_2 + 2e^- \rightarrow O_2^{\bullet-} \quad (10)$$

$$O_2^{\bullet-} + 2e^- + 2H^+ \rightarrow H_2O_2 \quad (11)$$

$$H_2O_2 + e^- \rightarrow {}^{\bullet}OH + OH^- \quad (12)$$

The practical applicability of $CuCo_2S_4$-based photocatalytic technology was evaluated in pharmaceutical wastewater from Jiangxi Chemedir Biopharm-Tech. Co., Ltd. As depicted in Fig. S11a (Supporting information), the COD value decreased from 60,500 mg/L (initial concentration) to 11,500 mg/L, and the TOC value dropped sharply from the initial concentration of 18,280 mg/L to 7465 mg/L. The COD and TOC removal efficiency of pharmaceutical wastewater reached 81.0% and 59.2% after 11 h visible-light photocatalysis, respectively (Figs. S11c and d in Supporting information). The satisfactory COD and TOC removal efficiency indicated universal applicability of the proposed $CuCo_2S_4$-based photocatalytic technology. To estimate the biodegradability enhancement of pharmaceutical wastewater by $CuCo_2S_4$-based photocatalytic technology, the carbon oxidation state (COS) and average oxidation state (AOS) change of pharmaceutical wastewater were studied during photocatalytic process. High COS and AOS values indicate high degree of reduction of organic matter (CH_4) and carbon oxidation (CO_2), respectively. COS and AOS were calculated according to the following Eqs. 13 and 14:

$$COS = 4 - 1.5\left[\frac{COD}{TOC_0}\right] \quad (13)$$

$$AOS = 4 - 1.5\left[\frac{COD}{TOC}\right] \quad (14)$$

where TOC_0 is the initial TOC concentration of pharmaceutical wastewater. The COS and AOS values keep increasing with photocatalysis going on (Fig. S11e in Supporting information), indicating that $CuCo_2S_4$-based photocatalytic technology can effectively improve the biodegradability of pharmaceutical wastewater.

In summary, three-dimensional hierarchical $CuCo_2S_4$ microspheres with asymmetric crystal structure were successfully prepared, and the lattice distortion of single-component $CuCo_2S_4$ was modulated by changing the feed Co/Cu molar ratio in synthesis. The relationship among lattice distortion, charge carrier separation and photocatalytic activity was established, and it was found that lattice expansion can promote charge carrier separation and boost photocatalytic performance. The optimized CCS-4 showed the maximum lattice expansion, and exhibited the highest photocatalytic activity with 95.4% of TC removal within 40 min photocatalysis, and maintained its photocatalytic stability in consecutive cycles. Additionally, CCS-4 can effectively remove COD and TOC of pharmaceutical wastewater, leading to biodegradability improvement of pharmaceutical wastewater. Importantly, this work inspires a new strategy for constructing single-component photocatalysts with perfect performance.

Declaration of competing interest

The authors declare that they have no known competing financial interests or personal relationships that could have appeared to influence the work reported in this paper.

Acknowledgments

This work was financially supported by the National Natural Science Foundation of China (Nos. 51978324, 51720105001, 51938007), Natural Science Foundation of Jiangxi Province (Nos. 20213BCJL22053, 20192ACBL20043, 20192ACBL21047), Natural Science Foundation of Jiangxi Province, China (No. 20212BAB204045), Key Laboratory of Jiangxi Province for Persistent Pollutants Control and Resources Recycle (Nanchang Hangkong University) (No. ES202002077).

Supplementary materials

Supplementary material associated with this article can be found, in the online version, at doi:10.1016/j.cclet.2022.04.066.

References

[1] I.L. Pepper, J.P. Brooks, C.P. Gerba, Environ. Sci. Technol. 52 (2018) 3949–3959.
[2] J. Chen, G.G. Ying, W.J. Deng, J. Agric. Food Chem. 67 (2019) 7569–7586.
[3] A.S. Oberoi, Y. Jia, H. Zhang, et al., Environ. Sci. Technol. 53 (2019) 7234–7264.
[4] P. Chaturvedi, B.S. Giri, P. Shukla, et al., Bioresour. Technol. 319 (2021) 124161.
[5] B. Xia, F. Deng, S. Zhang, et al., J. Hazard. Mater. 392 (2020) 122345.
[6] R. Lulijwa, E.J. Rupia, A.C. Alfaro, Rev. Aquacult. 12 (2020) 640–663.
[7] S.M. Limbu, L.Q. Chen, M.L. Zhang, et al., Rev. Aquac. 13 (2021) 1015–1059.
[8] J. Wang, X. Qin, J. Guo, et al., Water Res. 183 (2020) 116113.
[9] S. Dong, Y. Zhao, J. Yang, et al., Appl. Catal. B: Environ. 291 (2021) 120127.
[10] F. Polesel, H.R. Andersen, S. Trapp, et al., Environ. Sci. Technol. 50 (2016) 10316–10334.
[11] S. Terzic, N. Udikovic Kolic, T. Jurina, et al., J. Hazard. Mater. 349 (2018) 143–152.
[12] H. Cheng, P.Y. Hong, Environ. Sci. Technol. 51 (2017) 12200–12209.
[13] Z.H. Li, L. Yuan, S.X. Gao, et al., Water Res. 159 (2019) 145–152.
[14] S. Wang, X. Li, H. Zhao, et al., Water Res. 134 (2018) 162–169.
[15] G. Aylaz, M. Okan, M. Duman, et al., ACS Omega 5 (2020) 16635–16644.
[16] C. Guo, K. Wang, S. Hou, et al., J. Hazard. Mater. 323 (2017) 710–718.
[17] H. Li, F. Deng, Y. Zheng, et al., Environ. Sci. Nano 6 (2019) 3670–3683.
[18] Y. Deng, J. Liu, Y. Huang, et al., Adv. Funct. Mater. 30 (2020) 2002353.
[19] X. Jiang, L. Zhang, H. Liu, et al., Angew. Chem. Int. Ed. 59 (2020) 23112–23116.
[20] Q. Zhou, W. Huang, C. Xu, et al., Chem. Eng. J. 420 (2021) 129582.
[21] H. Li, Z. Su, S. Hu, et al., Appl. Catal. B: Environ. 207 (2017) 134–142.
[22] Y. Chen, J. Li, P. Liao, et al., Chin. Chem. Lett. 31 (2020) 1516–1519.
[23] W. Shi, H. Ren, M. Li, et al., Chem. Eng. J. 382 (2020) 122876.
[24] X. Li, B. Kang, F. Dong, et al., Nano Energy 81 (2021) 105671.
[25] J. Wang, Q. Zhang, F. Deng, et al., Chem. Eng. J. 379 (2020) 122264.
[26] C. Xu, Q. Zhou, W. Huang, et al., Rare Met. 41 (2022) 2094–2107.
[27] S. Bai, N. Zhang, C. Gao, et al., Nano Energy 53 (2018) 296–336.
[28] L. Yang, J. Guo, J. Zhang, et al., Chem. Eng. J. 427 (2022) 131550.
[29] X. Li, W. Wang, F. Dong, et al., ACS Catal. 11 (2021) 4739–4769.
[30] L. Yang, J. Guo, T. Yang, et al., J. Hazard. Mater. 402 (2021) 123741.
[31] W. Shi, F. Guo, S. Yuan, Appl. Catal. B: Environ. 209 (2017) 720–728.
[32] N.N. Vu, S. Kaliaguine, T.O. Do, Adv. Funct. Mater. 29 (2019) 1901825.
[33] X. Yan, Z. Jin, Chem. Eng. J. 420 (2021) 127682.
[34] L. Guo, Y. Chen, Z. Ren, et al., Ultrason. Sonochem. 81 (2021) 105849.
[35] Y. Fu, Z. Ren, J. Wu, et al., Appl. Catal. B: Environ. 285 (2021) 119785.
[36] R. Hailili, Z.Q. Wang, X.Q. Gong, et al., Appl. Catal. B: Environ. 254 (2019) 86–97.
[37] Y. Sun, H. Liao, J. Wang, et al., Nat. Catal. 3 (2020) 554–563.
[38] S. Lan, B. Jing, C. Yu, et al., Small 18 (2022) 2105279.
[39] S. Liu, B. Jing, C. Nie, et al., Environ. Sci. Nano 8 (2021) 784–794.
[40] Q. Liu, W. Zhao, Z. Ao, T. An, Chin. Chem. Lett. 33 (2022) 410–414.
[41] Y. Hu, Y. Pan, Z. Wang, et al., Nat. Commun. 11 (2020) 2129.
[42] H.J. Lee, S. Back, J.H. Lee, et al., ACS Catal. 9 (2019) 7099–7108.
[43] M. Chauhan, K.P. Reddy, C.S. Gopinath, et al., ACS Catal. 7 (2017) 5871–5879.
[44] A. Pendashteh, J.S. Sanchez, J. Palma, et al., Energy Storage Mater. 20 (2019) 216–224.
[45] S. Zhao, Y. Wang, Q. Zhang, et al., Inorg. Chem. Front. 3 (2016) 1501–1509.
[46] A.C. Riis Jensen, M. Pandey, K.S. Thygesen, J. Phys. Chem. C 122 (2018) 24520–24526.
[47] J. Ma, Trends Environ. Anal. Chem. 14 (2017) 37–43.
[48] F. Hillman, J.M. Zimmerman, S.M. Paek, et al., J. Mater. Chem. A 5 (2017) 6090–6099.
[49] J. Lin, H. Jia, H. Liang, et al., Chem. Eng. J. 336 (2018) 562–569.

[50] M. Wu, X. He, B. Jing, et al., J. Hazard. Mater. 384 (2020) 121323.
[51] M.A. Vishnuganth, N. Remya, M. Kumar, et al., J. Environ. Manag. 181 (2016) 201–207.
[52] D. Ollis, Appl. Catal. B: Environ. 242 (2019) 431–440.
[53] S. Vadivel, B. Paul, A. Habibi Yangjeh, et al., J. Phys. Chem. Solids 123 (2018) 242–253.
[54] Y. Chen, X. Ji, V. Sethumathavan, et al., Materials 11 (2018) 2303.
[55] K. Shahzad, M.B. Tahir, M. Sagir, et al., Ceram. Int. 45 (2019) 23225–23232.
[56] X. He, M. Wu, Z. Ao, et al., J. Hazard. Mater. 403 (2021) 124048.
[57] M. Wu, H. Lv, T. Wang, et al., Catal. Today 315 (2018) 205–212.
[58] P. Semeraro, S. Bettini, S. Sawalha, et al., Nanomaterials 10 (2020) 1458–1469.
[59] H. Wakayama, K. Hibino, K. Fujii, et al., Inorg. Chem. 58 (2019) 6161–6166.
[60] S. Huang, T. Ouyang, B. Zheng, M. Dan, Z. Liu, Angew. Chem. Int. Ed. 60 (2021) 9546–9552.
[61] S. He, C. Yan, X. Chen, et al., Appl. Catal. B: Environ. 276 (2020) 119138.
[62] S. Singh, C. Li, F. Panzer, et al., J. Phys. Chem. Lett. 7 (2016) 3014–3021.
[63] W. Wang, T. Ai, Q. Yu, Sci. Rep. 7 (2017) 42615.
[64] H. Yi, M. Yan, D. Huang, et al., Appl. Catal. B: Environ. 250 (2019) 52–62.
[65] Y. Wang, L. Li, Y. Zhang, et al., J. Phys. Chem. C 121 (2017) 19467–19477.
[66] A.M. Wiltrout, C.G. Read, E.M. Spencer, et al., Inorg. Chem. 55 (2016) 221–226.
[67] Z. Tian, X. Wang, B. Li, et al., Electrochim. Acta 298 (2019) 321–329.
[68] W. Zhang, B. Zhang, H. Jin, et al., Ceram. Int. 44 (2018) 20441–20448.
[69] L. An, Y. Li, M. Luo, et al., Adv. Funct. Mater. 27 (2017) 1703779.
[70] P. Zhao, Y. Liang, Y. Ma, et al., J. Phys. Chem. C 123 (2019) 4186–4192.
[71] B. Liu, L. Ning, C. Zhang, et al., Inorg. Chem. 57 (2018) 8019–8027.
[72] X. Hong, Q. Wang, Z. Tang, et al., J. Phys. Chem. C 120 (2016) 148–156.
[73] S. Chen, D. Huang, G. Zeng, et al., Chem. Eng. J. 382 (2020) 122840.
[74] A. Šuligoj, I. Arčon, M. Mazaj, et al., J. Mater. Chem. A 6 (2018) 9882–9892.
[75] F. Chen, J. Li, L. Xia, et al., Appl. Catal. B: Environ. 277 (2020) 119227.